Strong Electronic Interaction of Amorphous Fe₂O₃ Nanosheets with Single Atom Pt towards Enhanced Carbon Monoxide Oxidation

Wenlong Chen, Yanling Ma, Fan Li, Lei Pan, Wenpei Gao, Qian Xiang, Shang Wen, Chengyi Song, Peng Tao, Hong Zhu, Xiaoqing Pan, Tao Deng and Jianbo Wu*

W. Chen, Y. Ma, F. Li, L. Pan, Q. Xiang, Prof. W. Shang, Prof. C. Song, Prof. P. Tao, Prof. T. Deng, Prof. J. Wu

State Key Laboratory of Metal Matrix Composites, School of Materials Science and Engineering, Shanghai Jiao Tong University, 800 Dongchuan Road, Shanghai, 200240, P. R. E-mail: jianbowu@sjtu.edu.cn

Dr. W.Gao, Prof. X. Pan

Department of Chemical Engineering and Materials Science, University of California, Irvine, CA 92697, United States

Prof. H. Zhu

University of Michigan – Shanghai Jiao Tong University Joint Institute, Shanghai Jiao Tong University, 800 Dongchuan Road, Shanghai, 200240, P. R. China

Prof. T. Deng, Prof. J. Wu

Center of Hydrogen Science, Shanghai Jiao Tong University, 800 Dongchuan Road, Shanghai, 200240, P. R. China

Platinum-based catalysts are critical to lots of chemical processes, but their efficiency is not satisfying enough in some cases, because only the surface active-site atoms participate reaction. Henceforth, catalysts with single-atom dispersions are highly desirable to maximize their mass efficiency, but fabricating these structures with controllable method is still challenging. Most of the previous work focused on the crystalline materials. However, amorphous materials may have enhanced performance due to the distorted and isotropic nature of their disorder structure with numerous defects. Here we report a facile scale-up synthesis of atomically dispersed catalyst that consists of single Pt atoms and amorphous Fe_2O_3 nanosheets. Rational control can regulate the morphology from single atom, clusters to subnano-particles. The density functional theory calculation shows the synergistic effect resulted from the strong binding and stabilization of single Pt atoms with the strong metal-support interaction (SMSI) between the in-situ locally anchored Pt atoms and Fe_2O_3 lead to a weak CO adsorption. Moreover, the distorted amorphous Fe_2O_3 with O vacancies is beneficial for the activation of O_2, which further facilitated the CO oxidation on nearby Pt sites or interface sites between Pt and Fe_2O_3, resulting in the extremely high atom efficiency and high activity for CO oxidation of the atomic catalyst.

1. Introduction

In nowadays, catalysts have showed critical role for industrial and energy fields. Among the catalysts, the Pt has been proved one of the most widely used and most efficient materials. Supported metal nanostructures are the most widely used type of heterogeneous catalyst in industrial processes, especially for the Pt based ones. However, the high cost of Pt noble metal has limited its industrial applications. The size of catalyst plays an important role for the catalytic reactions and can make a huge difference of performance even the component of catalysts is the same. For the supported metal nanostructures, enormous efforts have contributed to improving the performance of supported metal catalysts by controlling the size of metal particles. However, for the most widely studied work, the usage of noble metals is still very high and on the other hand, the utilization efficiency of noble metals in these supported catalysts is far less than satisfactory. Recent reports have demonstrated that subnano clusters could have better catalytic performance and selectivity than the traditional nanometer-scale particles.[1] Low-coordinated, and unsaturated atoms often act

as active sites,[2] henceforth it is highly reasonable to downsize the particles or clusters to more dispersed single atoms in order to make use of each metal atom to achieve desirable catalysts for catalytic reactions. With this strategy in mind, it has called great interesting for the exploration of single atom catalysts in the past serval years since 2011,[1a] especially in nowadays. Till now, several kinds of single atom catalysts on substrates have been fabricated, such as Pt_1/FeO_x,[1a, 1b] Pt/ϑ-Al_2O_3,[3],[4] Au/CeO_2,[5] Pd/TiO_2,[6] Pt/CeO_2, Pd/Ru, Ir_1/FeO_x,[7] Au_1/FeO_x, Co/NG, Pt/Fe-N-C,[8] Pt/ZTC,[9] $Pt/Graphene$,[1c, 10] Pt-CN,[11] Pt/TiN,[12] $Pt/carbon$,[13] Fe-N_x,[14] Rh/CoO[15]. Although the single atom catalysts have shown attractive performances, wide employment is still hampered mainly due to the lack of readily available synthetic approaches with facile controllable methods and ultra-low loading (usually below 0.5%).[6, 16] Also, the most attention was focused on the single atom elements components, which were however supported in pre-prepared crystalized substrates. There is still very limited study to explore the roles of supports materials compared to the metal single atoms ingredients.

Crystalline catalysts or supports have been widely studied in the last decades years.[1a, 1b, 1d, 15, 17] However, their amorphous structures are still needed to be focused due to their unique structures and characteristics in many fields. For example, since the catalytic process for CO oxidation involves the participation of the supports, the number and activity of these supports active centers would be important factors for the catalytic performance. A distorted structure material would likely provide more such active sites and an amorphous structured-material surface may possess more oxygen vacancy which is beneficial for the CO oxidation process. [18] In light of this, amorphous oxides supports, which own much more distorted structure than crystalline ones, are able to possess higher catalytic activity for CO oxidation reaction. Furthermore, amorphous materials possess highly

3

homogeneous sites within a solid mixture down to the atomic scale, isotropic molecular diffusion and more percolation pathways, providing open framework and fast species diffusion.[18b, 19]

Here, we reported a facile method for the preparation of highly dispersed Pt single atom catalysts on amorphous Fe_2O_3 2D nanosheet substrates (Pt-SA/A-Fe_2O_3). The composites could be further precisely controlled from single atom, co-exist of single atom with subnano atoms clusters (Pt-SC/A-Fe_2O_3), to subnano nanoparticles Pt on Fe_2O_3 2D nanosheets (Pt-SN/A-Fe_2O_3) by different loading contents of Pt. We studied the synergetic influence between different size Pt and the amorphous Fe_2O_3 support on the efficiency of CO conversion. The Pt-SA/A-Fe_2O_3 catalyst showed extremely high activity for CO oxidation reactions, turning out to be the most active catalysts, with a low temperature around 70 ºC to achieve 100% CO conversion efficiency in comparison with the counterparts on crystalline support. The density functional theory (DFT) demonstrated the SMSI and adsorption energy varying with different sizes of Pt/supports. Especially, the synergy between the single atom structure and the amorphous Fe_2O_3 successfully weakens CO poisoning and promotes the activation of O_2 near the Pt and Fe_2O_3 surface, accelerating the CO oxidation kinetics. The study also revealed that the amorphous structure could be a practicable approach to enhance the catalytic performance of CO oxidation catalysts.

2. Results and discussion

2.1. Structural characterization of amorphous Fe_2O_3 supported different size Pt catalysts.

The Pt/Fe$_2$O$_3$ catalysts were prepared by a solvothermal method. The ethylene glycol (EG) is important for the formation of amorphous Fe$_2$O$_3$ nanosheets. [20] Unlike the layered materials, iron oxide phases, usually do not possess layered crystalline structures, henceforth, EG is needed to facilitate the formation of an amorphous Fe$_2$O$_3$ nanosheet rather than a nanoparticle form. [21] The effect of EG on facilitating the formation of iron oxide nanosheets may be related to the complexation of ethylene glycol with iron species during the dissociation and condensation reactions, as well as the suppress crystal growth along the other surfaces.[20, 22] By varying the amount of Pt loading and solvent, the dispersion and size of Pt metal were well controlled with their morphologies varying from isolated single atoms, loosely associated atoms clusters, sub-nano particles to three-dimensional (3D) large nanoparticles. **Figure 1a**, 1c and 1e present the representative TEM images of the as-prepared Pt-SA/A-Fe$_2$O$_3$, Pt-SC/A-Fe$_2$O$_3$, and Pt-SN/A-Fe$_2$O$_3$, respectively. The Pt-SA/A-Fe$_2$O$_3$ samples displayed a clean-surface nanosheets structure (Figure 1a), while the Pt-SC/A-Fe$_2$O$_3$ displayed dust-like points on surface (Figure 1c) and Pt-SN/A-Fe$_2$O$_3$ has small particles (1-2 nm) on the nanosheets substrates (Figure 1e). Moreover, the average thickness of the different catalysts nanosheets was ~3.1nm, according to the HAADF-STEM and HRTEM measurements for the thickness of the nanosheets, which is ultrathin to efficiently expose the active sites in catalytic reactions. (**Figure S1**) Figure 1b and insert showed the HAADF-STEM images of Pt-SA/A-Fe$_2$O$_3$, which can identify the heavy atoms.[1a, 13] As clearly revealed by bright spots contrasted with the dark substrate and marked by the red circles, isolated atoms were dispersed on the surface of Fe$_2$O$_3$ nanosheets (Figure 1b). All the Pt species existed almost only as isolated single atoms; neither subnanometre clusters nor big nanoparticles were observed (Figure 1b, more images from different regions can be found in **Figure S2**). On the contrary, when the Pt loading was more than

4.56 wt%, clustering of single atoms occurred and tiny clusters composed of loose and random ensembles of tens of atoms with dimensions 0.8-1.6 nm were formed (Figure 1d). Furthermore, when the Pt loading increased to 8.62 wt%, uniform small ripe sub-nanometer particles (~2nm) with occasional clusters were formed (Figure 1e-1f). These morphologies varying from single atoms, atoms clusters to sub-nano particles were further verified by X-ray photoelectron spectroscopy (XPS) and X-ray diffraction patterns (XRD) of Pt/Fe with different Pt mass loadings (**Figure 2**). **Figure S3** and Figure 2b showed the full XPS spectrum and Fe 2p region XPS spectrum with the detailed deconvoluted XPS peaks (**Figure S4**) of the three samples. All the three XPS spectra exhibited two peaks at ~711.3 eV and ~724.7 eV, which can be assigned to the Fe 2p 3/2 and Fe 2p 1/2 binding energies, respectively, indicating the oxidation status of Fe_2O_3.[18b, 23] The appearance of the small satellite peak in the XPS spectrum at ~719.0 eV can further confirm the existence of Fe_2O_3 in the as-synthesized catalysts.[23b] The XRD patterns in Figure 2a shows that for all the three samples, no crystalline Fe_2O_3 peaks could be observed, indicating the amorphous nature of the Fe_2O_3 supports. For the Pt-SA/A-Fe_2O_3, there is even none Pt diffraction peaks because of only single atom structures and extremely low mass loading which could not be detected.[1b] For the Pt-SC/A-Fe_2O_3, also very negligible signal of Pt can be found, in agreement with the form of tiny Pt clusters and aggregates composed by tens of Pt atoms. In Pt-SN/A-Fe_2O_3, the peaks of fcc Pt were clearly observed due to the existence of Pt ripe particles with ordered lattice, indicating the co-existence of Pt nanoparticles and the amorphous Fe_2O_3 in this catalyst.

We also carried out the HRTEM (Figure 2c-2e), selected area electron diffraction (SAED, Figure 2f-2h), and HAADF-STEM (Figure 2i-2k) images to investigate the detailed structure of the samples. As shown in Figure 2c-2e, for all the three samples, there are no clear crystal lattice fringes in the

Fe_2O_3 nanosheets. Furthermore, the SAED pattern images of the nanosheet supports also showed no strong diffraction rings or speckles ascribed to iron oxide. All these results also further proved the existence of amorphous-Fe_2O_3 supports. The magnified HAADF-STEM images in Figure 2i-2k revealed the single atoms, clusters and nanoparticles state of Pt on the amorphous Fe_2O_3 substrate, respectively.

2.2. X-ray absorption fine structure characterization and the local structure characterization.

The extended X-ray fine structure (EXAFS) and X-ray absorption near-edge spectroscopy (XANES) were carried out in order to further prove the Pt atom states and understand the specific local electronic structure of the single atom and cluster Pt catalysts (**Figure 3a-b, Figure S5**). The Pt K-edge XANES profiles in Figure 3a indicate that Pt species in Pt-SA/A-Fe_2O_3 were in a higher oxidation state than those in Pt-SC/A-Fe_2O_3 and Pt metallic foil, which was implied by the higher energy for absorption edge and the stronger intensity for the white line. [1a, 1b] As known to all, CO has strong adsorption on pure Pt metal catalysts, which blocks its catalytic sites, resulting in the poison effect. It has been reported the higher oxidation state of Pt species, the back-donating interaction between CO and Pt will be much less, and so the more-vacant d orbitals of the individual Pt atoms in catalyst play a vital role in the remarkable catalytic activity of the catalyst.[17c] It is worth noting that both the Pt-SA and Pt-SC catalysts showed peaks between the PtO_2 and Pt foil references. We can see that the Pt single atom displayed the highest oxidation state than the cluster structure and metallic nanoparticle, and henceforth this will weaken the interaction of CO and Pt, and also activate the C-O bond. Furthermore, as shown in EXAFS in R space (Figure 3b), Pt-SA/A-Fe_2O_3 exhibited a prominent

peak at ca. 1.7 Å from the Pt-O shell contribution. No other obvious typical peaks for Pt-Pt contribution at were observed. Thus, Pt single atoms were finely dispersed throughout the entire amorphous Fe_2O_3 substrate. The fitting EXAFS curves were shown in **Figure S6**, and the fitting EXAFS parameters and the coordination environment results for platinum was summarized Table S2. The fitted Pt–O coordination number for Pt-SA/A-Fe_2O_3 is ~4.1, indicating that each Pt atom coordinates with four oxygen atoms on the Fe_2O_3 support, what's more, it is reported this four-coordination structure is inherently preferred by zero or low valent Pt complexes, which may partially explain the good stability of the Pt single-atom catalyst in the catalysis, and the Pt–O bonding distance is close to that in PtO_2 suggests the strong metal–support interaction.[1a, 24] When the Pt loading was increased to 4.56 wt% (Pt-SC/A-Fe_2O_3), there was also a prominent peak in the range of ~1.5-1.8 Å, and a very slight raised peak at~2.8 Å can be carefully observed, implying that the clusters with nearby Pt interactions started to appear (Figure 3j). However, their Pt-Pt coordination and shell were still relatively low compared with that of Pt foil, similar with that of Pt-SA/A-Fe_2O_3 catalyst, indicating the formation of very small (1.0 nm) Pt clusters composed by irregular Pt atoms. All of the above XAFS results are in consistent with the observation of the shape from the HAADF-STEM (Figure 2).

The inductively coupled plasma mass spectrometry (ICP-MS) was applied to investigate the loading of Pt, showing results of as high as 1.2wt % for Pt-SA/A-Fe_2O_3, 4.56wt% of Pt in Pt-SC/A-Fe_2O_3 and 8.62wt% for Pt-SN/A-Fe_2O_3 (Table S1), in consistent with the result trend obtained by the HAADF-STEM. EDS mapping analysis in a HAADF-STEM revealed the evenly dispersed Pt and Fe in the Pt-SA and Pt-SC/A-Fe_2O_3 (Figure 3c-3d). Correspondingly, the STEM-EDS of Pt-SN/A-Fe_2O_3 further proved the form of sub-nano Pt particles on the nanosheets (Figure 3e). The thickness of the single

atom or sub-nano Pt dispersed nanosheets is estimated ~ 1.4 nm from the aberration-corrected HAADF-STEM and HRTEM images of the side edge.

2.3. Phase-transformation of the amorphous substrate to crystalline supports

It should be noted that the single atoms of Pt were stabilized at a high concentration of 1.2 wt% in our synthetic process, probably due to the SMSI of the amorphous Fe_2O_3 nanosheets. Therefore, this 2D Fe structure benefit for oxidation reaction.[25] According to the above results from both HAADF-STEM and XANES/EXAFS, we have prepared three kinds of Pt structures anchored onto the amorphous Fe_2O_3 nanosheets, and in order to make a detailed comparison of the CO oxidation behavior between the amorphous and crystalline Fe_2O_3 supported catalyst, at the same time we also transformed the amorphous Fe_2O_3 support to crystalized ones and got the other three kind of catalysts via annealing at 300 ^{o}C, named Pt-SA/C-Fe_2O_3, Pt-SC/C-Fe_2O_3 and Pt-SN/C-Fe_2O_3. As can be seen from the **Figure 4a**, after annealing process, all the XRD patterns of the three Pt/Fe_2O_3 catalysts displayed obviously Fe_2O_3 diffraction peaks, indicating the formation of Fe_2O_3 crystallized structure, in good agreement with the typical high-resolution HRTEM (Figure 4b, 4d, and 4f) and the corresponding magnified HAADF-STEM images in Figure 4c, 4e and 4g, which exhibited clearly crystal lattice fringes in the 2D sheets structures of Fe_2O_3. In detail, as depicted in the HAADF-STEM images (Figure 4c, 4e, and 4g) corresponding to the Pt single atom, cluster and nanoparticle on Fe_2O_3 after annealing, it is worth noting that the Pt state on the fine latticed supports by annealing treatment was not obviously impacted and nearly the same as their atomic structures in the amorphous Fe_2O_3. Henceforth, combining the above three Pt/A-Fe_2O_3 and the three Pt/C-Fe_2O_3 catalysts, we have good

model catalysts to study the structure–function relations for the different sized platinum catalysts and the amorphous/crystalline supports effects towards CO oxidation reaction.

2.4. CO Oxidation on different catalysts.

CO oxidation experiments were carried out at a fixed flow mixture of CO, O_2, and N_2 at a constant hourly space velocity (constant weight of catalyst). CO oxidation on Pt-SA/A-Fe_2O_3, Pt-SC/A-Fe_2O_3 and Pt-SN/A-Fe_2O_3 initiate at approximately 10, 20, and 50°C, respectively (**Figure 5**). Correspondingly, the initiating temperature for the Pt-SA/C-Fe_2O_3, Pt-SC/C-Fe_2O_3 and Pt-SN/C-Fe_2O_3 were approximately at 30°C, 30°C and 50°C. The results clearly show that Fe_2O_3-supported single Pt atoms or atomic clusters are catalytically active for the oxidation of CO at room temperature. In addition, the CO oxidation is easier in low temperature for the amorphous Fe_2O_3 supported Pt catalysts than their crystalline ones. For example, at 30 °C, the Pt-SA/A-Fe_2O_3 converted CO by ~20% while the crystalline counterpart (Pt-SA/C-Fe_2O_3) converted CO only 8%. Furthermore, the CO conversation of the different samples differed from each other significantly. As shown in Figure 5, the CO conversation achieved to 100% at near 70 °C for the Pt-SA/A-Fe_2O_3 catalyst, and those T_{100} (the lowest temperatures to reach 100% efficiency of CO conversion) for Pt-SC/A-Fe_2O_3, Pt-SN/A-Fe_2O_3 are ~80 °C and ~110 °C, respectively. However, for the Pt-SA/C-Fe_2O_3, Pt-SC/C-Fe_2O_3 and Pt-SN/C-Fe_2O_3 catalysts, the T_{100} are ~80°C, ~100°C and 125°C, which were higher than their amorphous forms by ~10 °C, ~20°C and 15°C, respectively. These results also confirm the more active performance of single atom catalyst, as well as indicating the amorphous Fe_2O_3 support is beneficial

for the CO oxidation. To further investigate the active performance, the specific rate at 60 ºC was measured according to the average activity at 20, 40 and 60 min. Additionally, the corresponding turnover frequency (TOF) of the catalysts was also calculated to obtain the intrinsic activity for further comparison of their size effects and supports influence. As shown in Table 1, the Pt-SA/A-Fe$_2$O$_3$ gave a specific reaction rate of 1.25 mol$_{CO}$ h^{-1} g$_{Pt}^{-1}$ at the reaction temperature of 70 ^{o}C, which is 7.1 times that of Pt-SC/A-Fe$_2$O$_3$ catalyst and almost 26.4 times than that of Pt-SN/A-Fe$_2$O$_3$. As expected, it implied a slower specific rate for the crystalline Fe$_2$O$_3$ supported Pt (Table 1), which shows that the Pt-SA/A-Fe$_2$O$_3$ is 1.53 time of the Pt-SA/C-Fe$_2$O$_3$ towards the specific rate. What's more, the other two kinds of Pt on crystalline Fe$_2$O$_3$ exhibited poorer specific rate than the amorphous forms. The TOFs also showed that Pt-SA/A-Fe$_2$O$_3$ was 7 times and 26.4 times more active than Pt-SC/A-Fe$_2$O$_3$ and Pt-SN/A-Fe$_2$O$_3$. Further study on TOFs for the crystalline Fe$_2$O$_3$ supported Pt also indicated the superior performance of amorphous materials (Table 1). All these results indicated that our Pt-SA catalyst was the most active for CO oxidation among the different sized Pt catalysts from single atom to nanoparticles and the amorphous Fe$_2$O$_3$ structure is beneficial for the rapid CO oxidation. It can be found that our work exhibited comparable performance towards the other reports on superior CO oxidation catalysts to date (Table S3). The high activity of single atom catalyst on the amorphous supports must have originated from the intrinsic nature of single Pt atoms dispersed onto Fe$_2$O$_3$ surfaces. We further investigated the long-term-use stability of the Pt-SA/A-Fe$_2$O$_3$ catalyst. The morphology and the structure state of the atomically dispersed Pt-SA/A-Fe$_2$O$_3$ catalyst using HAADF-STEM, HRTEM and SAED after the CO oxidation test (**Figure S7**). As a result, the single-atomic dispersion of Pt was still well maintained without aggregation, Moreover, the HRTEM did not show any crystalline lattices after the CO oxidation and the further SAED image still display

no obvious diffraction rings or speckles as its original state before CO oxidation, suggesting the retained amorphous structure of the Fe_2O_3 in Pt-SA/A-Fe_2O_3. In addition, the CO oxidation performance of the Pt-SA/A-Fe_2O_3 catalyst after the stability test showed that the CO conversion at different temperatures was similar before and after the 30h stability test **(Figure S8-S9)**. Specifically, the CO conversion at 70℃ was 93.8% after 30h, giving a specific reaction rate of 1.17 mol_{CO} h^{-1} g_{Pt}^{-1}, indicating no obvious degradation compared to the performance at 0h (97.2%, 1.25 mol_{CO} h^{-1} g_{Pt}^{-1}). All these results suggested the good stability of the Pt-SA/A-Fe_2O_3 catalyst.

2.5. Understanding of Relation between Catalytic Activity and Catalysts Surface Properties.

To elucidate the nature of the exceptionally high catalytic activity of Pt single atom catalyst on the amorphous Fe_2O_3, relativistic DFT calculations were carried out to give extensive theoretical investigations. To explore the interfacial interaction of the Pt species with the Fe_2O_3, we studied the charge interaction between them by using the Bader charge analysis method (**Figure 6a-6c**). As expected, electron transfer occurs from different Pt species to the Fe_2O_3 surfaces, leading to a positive charge on Pt. This electron transfer leads to the stronger interfacial interactions, which has been reported as an important influence on surface reactivity.[1a, 26] [27]The Bader charge analysis revealed that the amount of charge transfer (Δq) is 0.746, 0.221, and 0.114 eV/atom for Pt SA, SC and SN on the amorphous Fe_2O_3 surfaces (Table S4), respectively, indicating that the strongest interfacial interaction between Pt-SA and Fe_2O_3 than the other catalysts, which was in consistent with the CO oxidation performance. The binding energy of Pt species with Fe_2O_3 (Figure 6d and Table S5) also proved the strongest interaction of Pt SA with the Fe_2O_3. To further reveal the nature of the

high reactivity on Pt-SA/A-Fe$_2$O$_3$, we calculated adsorption energy for CO and O$_2$ (Figure 6e and Table S6). The adsorption energy of CO appears a tendency of increasing while the stable adsorption energy of O$_2$ decreases remarkably in the order of Pt-SA/A-Fe$_2$O$_3$, Pt-SC/A-Fe$_2$O$_3$ to Pt-SN/A-Fe$_2$O$_3$. This is a clear demonstration that the CO poisoning effect of Pt-SA/A-Fe$_2$O$_3$ is the weakest and the activation of O$_2$ for Pt-SA/A-Fe$_2$O$_3$ is the strongest, both leading to a highest CO oxidation performance of the Pt-SA/A-Fe$_2$O$_3$ catalyst. To further prove the CO adsorption performance, the electrochemical CO stripping experiments were carried out for the above three samples, which can be seen in **Figure S10**. It definitely showed the peak density of CO oxidation in the sequence Pt-SA/A-Fe$_2$O$_3$＜Pt-SC/A-Fe$_2$O$_3$＜ Pt-SC/A-Fe$_2$O$_3$. Furthermore,the peak potential positions were 0.713 V, 0.718 V and 0.738 V for these three samples, respectively, indicating the weakest CO adsorption on Pt single atoms. For the Pt-SC and Pt-SN catalysts, their CO adsorption was stronger and the O$_2$ interaction was much reduced, both of which lead to a suppressed CO oxidation. The d-band center of Fe shows down-shift trends for Pt-SA/A-Fe$_2$O$_3$, Pt-SC/A-Fe$_2$O$_3$ to Pt-SN/A-Fe$_2$O$_3$ (Figure 6f-6g, **Fig S11-S12**, and Table S7), indicating the decreased O$_2$ interaction, agreeing with the calculated adsorption energy. Moreover, to further understand the effect from the oxygen vacancy structure conditions in the two kinds of supports, electron paramagnetic resonance (EPR) was used to detect the unpaired electrons in the Pt-SA/A-Fe$_2$O$_3$ and Pt-SA/C-Fe$_2$O$_3$ samples (**Figure S13**). It can be seen Pt-SA/A-Fe$_2$O$_3$ exhibited a signal at g value of 2.003 (Figure S13), which could be identified as the electrons trapped on O-vacancies, suggesting that abundant oxygen vacancies emerged on the surface of Pt-SA/A-Fe$_2$O$_3$. It has been widely reported that the O$_2$ activation was more efficient in the amorphous surface with more vacancies and distorted active sites than the crystalline supported one,[28] which well explained the superior performance of Pt-SA/A-Fe$_2$O$_3$ than that of Pt-SA/C-Fe$_2$O$_3$.

Based on our study, it is believed the CO oxidation for the Pt/Fe_2O_3 was catalyzed in a Langmuir-Hinshelwood pathway, and the reaction mechanism for the $Pt-SA/A-Fe_2O_3$ can be described as Figure 6h. It has been reported that the CO oxidation reaction of Pt catalysts over non-supports occurs very slowly at low temperature because oxygen adsorption can easily be blocked by a saturated layer of adsorbed CO on the Pt surface.[29] However, when supported on iron oxides substrate materials, the Pt metal will play the role in adsorbing and active CO molecule, while the Fe_2O_3 substrates will be considered to activate the O_2 from the gas environment in relatively low temperature. Subsequently, the activated CO will react with the active O species to form CO_2 and finish the CO oxidation process.[30] In our work, the amorphous Fe_2O_3 played two critical roles which were beneficial for the CO oxidation. On the one hand, the Fe_2O_3 interacted with the Pt species will induce strong metal–support interactions, which could change the state of Pt. As can be seen from the XANES results (Figure 3a), the Pt in $Pt-SA/A-Fe_2O_3$ existed with high oxidation state, indicating the presence of high-valence Pt atoms, which could help to reduce the CO adsorption energy for CO oxidation, [2] which is also indicated by DFT in Figure 6. On the other hand, the amorphous Fe_2O_3 substrate with abundant oxygen vacancies was beneficial for the activation of the O_2 near the catalysts surface from the supplying hybrid gas. The abundant and easier-produced active O species will react with the CO adsorbed near the Pt to form CO_2, which as a result, accelerated the CO oxidation process.[28b, 28c, 31] In addition, the distorted structure would likely provide more such active sites for reaction, [19b, 28a, 32] which exhibit isotropic molecular diffusion and supply more percolation pathways to accelerate the fast diffusion of gas species in the process [18b].

3. Conclusion

In summary, we reported a series of Pt catalysts on amorphous structure Fe_2O_3 ultra nanosheets from single atoms, clusters to subnano particles with the different loading contents of Pt. The atomically dispersed Pt single atoms on ultrathin amorphous Fe_2O_3 nanosheets show great promise for catalysis due to the high specific surface area, full exposed atoms sites and the synergistic effect between the atomically dispersed Pt single atoms and the amorphous Fe_2O_3 supports which could easily active the CO oxidation, as well as its open framework and fast diffusion for the reacting gas species.[18b, 23a, 28c, 33] Furthermore, we compared the CO oxidation performance among the size effect as well as the support effect between amorphous and crystalline forms. Specifically, the Pt-SA/A-Fe_2O_3 catalyst showed extremely superior activity for CO oxidation reactions because: 1) the strong binding and stabilization of single Pt atoms coming from the SMSI between the in-situ locally synthesized Pt atoms and Fe_2O_3 supports; 2) the single atom configuration leads to a weak CO adsorption on Pt and an enhanced O_2 adsorption on nearby Fe_2O_3; 3) the very close neighbored amorphous Fe_2O_3 species substrate possess many defects and O-vacancies is easy to interact with oxygen and provide active abundant sites to activate huge amount of O due to its specific characteristic, which could further facilitate the CO_{ad} oxidation on the neighboring Pt or the interface between Pt and Fe_2O_3. All of these synergistic effects ultimately account for the excellent catalytic activity. Our study provides a promising facile approach for the synthesis of highly active and stable single-atom catalysts with amorphous supports based on single Pt atoms and clusters, which have a great potential to reduce the high cost of industrial, commercial noble-metal catalysts in many applications or industry.

15

4. Experimental Section

Chemicals and Materials: Platinum(II) acetylacetonate (Pt(acac)$_2$, Strem Chemical, 98%), Iron(III) acetylacetonate (Fe(acac)$_3$, Strem Chemical, 98%), tungsten hexacarbonyl (W(CO)$_6$, Strem Chemical, 99%), ethylene glycol (EG, Sinopharm Chemical Reagent Co., Ltd, AR), N,N-dimethylformamide (DMF, Sinopharm Chemical Reagent Co., Ltd, AR). Carbon monoxide (CO, 5%), oxygen (O$_2$, 5%), nitrogen (N$_2$, 99.999%) and argon (Ar, 99.999%) were purchased from Shanghai Weichuang Standard Gas Analytical Technology Co., Ltd.

Synthesis of Pt single atoms on amorphous Fe$_2$O$_3$ nanosheets: In a typical synthesis, Pt(acac)$_2$ (0.025 mmol), Fe(acac)$_3$ (3.14 mmol), 150 mg W(CO)$_6$ were mixed into 15 mL of ethylene glycol under room temperature under stirring. After the precursors were dissolved, then the mixed solution was transferred to the Teflon-lined stainless-steel autoclaves and heated at 120 ºC for 42 h. The final product was washed and collected with ethanol, DI water, and acetone for two times, by centrifugation at 8000 rpm for 5 min, respectively. The above product was then transferred to a 60 °C oven in air condition for 6 hours, and this product was used as the catalysts for the CO oxidation.

Synthesis of Pt single atoms with clusters on amorphous Fe$_2$O$_3$ nanosheets and Pt sub-nano particles on amorphous Fe$_2$O$_3$ nanosheets: The method was similar as the single atom catalyst, except the usage of Pt(acac)$_2$ is 0.075 mmol and 0.12 mmol, respectively.

Transformation of amorphous substrate to crystalline Fe$_2$O$_3$ phase: The above-obtained Pt/A-Fe$_2$O$_3$ materials were then annealed in a glass tube furnace at 300 °C for 30 min in Ar condition and collected the products for characterization.

Characterization. The loadings of Pt were measured on inductively coupled plasma spectrometer on a 6300 instrument (Thermo Electron Corp.). XRD patterns were recorded by using a SmartLab with Cu Kα radiation (λ=1.54178Å). The TEM was carried out on a JEM-2800, and a JEM-2100F field emission electron microscope at an acceleration voltage of 200 kV. The high-resolution TEM, HAADF-STEM and the corresponding energy dispersive spectroscopy mapping analyses were performed on a JEOL JEM-ARM200F S/TEM with a spherical aberration corrector and Grand ARM S/TEM at 300 kV with both image and probe corrector.

The X-ray absorption fine structure measurements (XAFS): XAFS data of the samples over Pt L_3-edge were collected in transmission mode at the Advanced Photon Source located within the Argonne National Laboratory (Beamline 20 BM). Pt foil and PtO_2 were used as reference samples and measured in the transmission mode. XAS data were processed and analyzed using Athena and Artemis. For the X-ray absorption near-edge structure (XANES) part, the experimental absorption coefficients as function of energies m(E) were processed by background subtraction and normalization procedures, which were reported as 'normalized absorption'.

CO oxidation catalytic tests. The catalytic performances of samples for CO oxidation were evaluated in a fixed-bed reactor. The powder samples were packed between quartz wool with a thermocouple placed touching the sample inside the reactor. Prior to the tests, the samples were pelletized and sieved to 60 mesh for use. Approximately 60 mg of the samples and diluted with about 1 g of SiO_2 powder were loaded into a straight-shaped quartz reactor. The feed gas containing 1 vol% CO, 1 vol% O_2 and balance N_2 was allowed to pass through the reactor at a flow rate of 18.75 ml min^{-1} (corresponding to a space velocity of 18750 ml h^{-1} g$_{cat}^{-1}$). The effluent gas compositions were analyzed on-line by a gas chromatograph (GC-2014, Shimadzu). The CO conversions were calculated

based on the difference between inlet and outlet concentrations. The CO oxidation long-term stability for the highest performance Pt-SA/A-Fe$_2$O$_3$ catalyst was as follows. The Pt-SA/A-Fe$_2$O$_3$ catalyst was treated to continuously catalyze the CO oxidation under the same CO oxidation operating conditions in 80 ℃ (in the temperature of the complete 100% CO conversion), and in the same presence of other environmental conditions (such as 1 vol% CO, 1 vol% O$_2$ and balance N$_2$). After 30h treatment, the CO oxidation performance was explored again to compare with its initial state.

Turnover frequency (TOF) Measurements and Calculation: The specific reaction rates and TOFs of the catalyst were obtained at specific temperatures CO conversion used to calculate the TOF and reaction rate was the average of three results at 20, 40 and 60 min. The dispersion of single atom catalyst was 100% and those of other Pt/Fe$_2$O$_3$ were calculated according to D=0.9/d_{Pt}, where d means the average diameter of supported Pt clusters.

DFT calculation methods: we provide a detailed description of computational models and methods. Our DFT calculations were performed using the Vienna Ab initio Simulation Package (VASP)[34] code with the PW91 generalized gradient approximation (GGA)[35], projector-augmented wave (PAW)[36] pseudopotentials and a cut-off energy of 520 eV for the plane-wave expansion of the wave functions. Ground-state atomic geometries were obtained by minimizing the total free energy change and the band structure energy change between two steps both smaller than 1*10^{-4} eV. To model Pt-SA/A-Fe$_2$O$_3$, Pt-SC/A-Fe$_2$O$_3$, and Pt-SN/A-Fe$_2$O$_3$, we chose single Pt atom, Pt cluster consisting of three atoms, and Pt nanoparticle consisting of ten atoms with half of wulff structure, on the amorphous Fe$_2$O$_3$ model, respectively. A Monkhorst-Pack grid of size of 1×1×1 was used to

WILEY-VCH

sample the surface Brillouin zone[37], and the repeated slabs were separated from their neighboring images by a 15 Å-width vacuum in the direction perpendicular to the surface.

Supporting Information

Supporting Information is available from the Wiley Online Library or from the author.

Received: ((will be filled in by the editorial staff))
Revised: ((will be filled in by the editorial staff))
Published online: ((will be filled in by the editorial staff))

References

[1]   a) B. T. Qiao, A. Q. Wang, X. F. Yang, L. F. Allard, Z. Jiang, Y. T. Cui, J. Y. Liu, J. Li, T. Zhang, *Nat. Chem.* **2011**, *3*, 634; b) H. S. Wei, X. Y. Liu, A. Q. Wang, L. L. Zhang, B. T. Qiao, X. F. Yang, Y. Q. Huang, S. Miao, J. Y. Liu, T. Zhang, *Nat. Commun.* **2014**, *5,* 5634; c) H. Yan, Y. Lin, H. Wu, W. H. Zhang, Z. H. Sun, H. Cheng, W. Liu, C. L. Wang, J. J. Li, X. H. Huang, T. Yao, J. L. Yang, S. Q. Wei, J. L. Lu, *Nat. Commun.* **2017**, *8,* 1070; d) J. Jones, H. F. Xiong, A. T. Delariva, E. J. Peterson, H. Pham, S. R. Challa, G. S. Qi, S. Oh, M. H. Wiebenga, X. I. P. Hernandez, Y. Wang, A. K. Datye, *Science* **2016**, *353*, 150; e) B. T. Qiao, A.

Q. Wang, L. Li, Q. Q. Lin, H. S. Wei, J. Y. Liu, T. Zhang, *ACS Catal.* **2014**, *4*, 2113.

[2]   X. F. Yang, A. Q. Wang, B. T. Qiao, J. Li, J. Y. Liu, T. Zhang, *Acc. Chem. Res.* **2013**, *46*, 1740.

[3]   Z. Y. Li, Z. Yuan, X. N. Li, Y. X. Zhao, S. G. He, *J. Am. Chem. Soc.* **2014**, *136*, 14307.

[4]   M. Moses-DeBusk, M. Yoon, L. F. Allard, D. R. Mullins, Z. L. Wu, X. F. Yang, G. Veith, G. M. Stocks, C. K. Narula, *J. Am. Chem. Soc.* **2013**, *135*, 12634.

[5]   L. W. Guo, P. P. Du, X. P. Fu, C. Ma, J. Zeng, R. Si, Y. Y. Huang, C. J. Jia, Y. W. Zhang, C. H. Yan, *Nat. Commun.* **2016**, *7,* 13481.

[6]   P. X. Liu, Y. Zhao, R. X. Qin, S. G. Mo, G. X. Chen, L. Gu, D. M. Chevrier, P. Zhang, Q. Guo, D. D. Zang, B. H. Wu, G. Fu, N. F. Zheng, *Science* **2016**, *352*, 797.

[7]   J. Lin, A. Q. Wang, B. T. Qiao, X. Y. Liu, X. F. Yang, X. D. Wang, J. X. Liang, J. X. Li, J. Y. Liu, T. Zhang, *J. Am. Chem. Soc.* **2013**, *135*, 15314.

[8]   X. J. Zeng, J. L. Shui, X. F. Liu, Q. T. Liu, Y. C. Li, J. X. Shang, L. R. Zheng, R. H. Yu, *Adv. Energy Mater.* **2018**, *8,* 1701345.

[9]   C. H. Choi, M. Kim, H. C. Kwon, S. J. Cho, S. Yun, H. T. Kim, K. J. J. Mayrhofer, H. Kim, M. Choi, *Nat. Commun.* **2016**, *7,* 10922.

[10]   N. C. Cheng, S. Stambula, D. Wang, M. N. Banis, J. Liu, A. Riese, B. W. Xiao, R. Y. Li, T. K. Sham, L. M. Liu, G. A. Botton, X. L. Sun, *Nat. Commun.* **2016**, *7,* 13638.

[11]   X. G. Li, W. T. Bi, L. Zhang, S. Tao, W. S. Chu, Q. Zhang, Y. Luo, C. Z. Wu, Y. Xie, *Adv. Mater.* **2016**, *28*, 2427.

[12]   S. Yang, J. Kim, Y. J. Tak, A. Soon, H. Lee, *Angew. Chem.* **2016**, *128*, 2098; *Angew. Chem. Int. Ed.* **2016**, *55*, 2058.

[13]   H. H. Wei, K. Huang, D. Wang, R. Y. Zhang, B. H. Ge, J. Y. Ma, B. Wen, S. Zhang, Q. Y. Li, M. Lei, C. Zhang, J. Irawan, L. M. Liu, H. Wu, *Nat. Commun.* **2017**, *8,* 1490.

[14]   P. Z. Chen, T. P. Zhou, L. L. Xing, K. Xu, Y. Tong, H. Xie, L. D. Zhang, W. S. Yan, W. S. Chu, C. Z. Wu, Y. Xie, *Angew. Chem.* **2017**, *129*, 625; *Angew. Chem. Int. Ed.* **2017**, *56*, 610.

[15]   L. B. Wang, W. B. Zhang, S. P. Wang, Z. H. Gao, Z. H. Luo, X. Wang, R. Zeng, A. W. Li, H. L. Li, M. L. Wang, X. S. Zheng, J. F. Zhu, W. H. Zhang, C. Ma, R. Si, J. Zeng, *Nat. Commun.* **2016**, *7,* 14036.

[16]   C. Z. Zhu, S. F. Fu, Q. R. Shi, D. Du, Y. H. Lin, *Angew. Chem.* **2017**, *129*, 14132; *Angew. Chem. Int. Ed.* **2017**, *56*, 13944.

[17]   a) J. Kim, C. W. Roh, S. K. Sahoo, S. Yang, J. Bae, J. W. Han, H. Lee, *Adv. Energy Mater.* **2018**, *8,* 1701476; b) H. L. Li, L. B. Wang, Y. Z. Dai, Z. T. Pu, Z. H. Lao, Y. W. Chen, M. L. Wang, X. S. Zheng, J. F. Zhu, W. H. Zhang, R. Si, C. Ma, J. Zeng, *Nat. Nanotechnol.* **2018**, *13*, 411; c) L. Lin, S. Yao, R. Gao, X. Liang, Q. Yu, Y. Deng, J. Liu, M. Peng, Z. Jiang, S. Li, Y.-W. Li, X.-D. Wen, W. Zhou, D. Ma, *Nat. Nanotechnol.* **2019**, DOI: 10.1038/s41565-019-0366-5.

[18]   a) L. Wei, H. E. Karahan, S. L. Zhai, H. W. Liu, X. C. Chen, Z. Zhou, Y. J. Lei, Z. W. Liu, Y. Chen, *Adv. Mater.* **2017**, *29,* 1701410; b) Y. Z. Jiang, D. Zhang, Y. Li, T. Z. Yuan, N. Bahlawane, C. Liang, W. P. Sun, Y. H. Lu, M. Yan, *Nano Energy* **2014**, *4*, 23; c) W. C. Xu, H. X. Wang, *Chin. J. Catal.* **2017**, *38*, 991.

[19]   a) S. Q. Liu, H. R. Wen, Ying-Guo, Y. W. Zhu, X. Z. Fu, R. Sun, C. P. Wong, *Nano Energy* **2018**, *44*, 7; b) J. S. Yang, J. J. Xu, *Electrochem. Commun.* **2003**, *5*, 306; c) B. R. Goldsmith, B. Peters, J. K.

Johnson, B. C. Gates, S. L. Scott, *ACS Catal.* **2017**, *7*, 7543.

[20]   S. Niu, R. McFeron, F. Godinez-Salomon, B. S. Chapman, C. A. Damin, J. B. Tracy, V. Augustyn, C. P. Rhodes, *Chem. Mater.* **2017**, *29*, 7794.

[21]   a) Y. Zhao, L. L. Peng, B. R. Liu, G. H. Yu, *Nano Lett.* **2014**, *14*, 2849; b) P. Z. Chen, K. Xu, X. L. Li, Y. Q. Guo, D. Zhou, J. Y. Zhao, X. J. Wu, C. Z. Wu, Y. Xie, *Chem. Sci.* **2014**, *5*, 2251.

[22]   X. Qin, J. M. Wang, J. Xie, F. Z. Li, L. Wen, X. H. Wang, *PCCP* **2012**, *14*, 2669.

[23]   a) D. Li, J. S. Zhou, X. H. Chen, H. H. Song, *ACS Appl. Mat. Interfaces* **2016**, *8*, 30899; b) Y. Huang, Z. X. Lin, M. B. Zheng, T. H. Wang, J. Z. Yang, F. S. Yuan, X. Y. Lu, L. Liu, D. P. Sun, *J. Power Sources* **2016**, *307*, 649.

[24]   Z. L. Zhang, Y. H. Zhu, H. Asakura, B. Zhang, J. G. Zhang, M. X. Zhou, Y. Han, T. Tanaka, A. Q. Wang, T. Zhang, N. Yan, *Nat. Commun.* **2017**, *8,* 16100.

[25]   D. H. Deng, K. S. Novoselov, Q. Fu, N. F. Zheng, Z. Q. Tian, X. H. Bao, *Nat. Nanotechnol.* **2016**, *11*, 218.

[26]   L. DeRita, J. Resasco, S. Dai, A. Boubnov, H. V. Thang, A. S. Hoffman, I. Ro, G. W. Graham, S. R. Bare, G. Pacchioni, X. Pan, P. Christopher, *Nat. Mater.* **2019**, DOI: 10.1038/s41563-019-0349-9.

[27]   Y. Zhou, D. E. Doronkin, M. L. Chen, S. Q. Wei, J. D. Grunwaldt, *ACS Catal.* **2016**, *6*, 7799.

[28]   a) P. W. Cai, J. H. Huang, J. X. Chen, Z. H. Wen, *Angew. Chem*. **2017**, *129,* 4936; *Angew. Chem. Int. Ed.* **2017**, *56*, 4858; b) F. C. Lei, Y. F. Sun, K. T. Liu, S. Gao, L. Liang, B. C. Pan, Y. Xie, *J. Am. Chem. Soc.* **2014**, *136*, 6826; c) D. F. Yan, Y. X. Li, J. Huo, R. Chen, L. M. Dai, S. Y. Wang, *Adv. Mater.* **2017**, *29*;

d) S. H. Ye, Z. X. Shi, J. X. Feng, Y. X. Tong, G. R. Li, *Angew. Chem.* **2018**, *130*, 2702; *Angew. Chem. Int. Ed.* **2018**, *57*, 2672.

[29]   L. Xu, X. C. Xu, L. K. Ouyang, X. J. Yang, W. Mao, J. J. Su, Y. F. Han, *J. Catal.* **2012**, *287*, 114.

[30]   a) K. Liu, A. Q. Wang, T. Zhang, *ACS Catal.* **2012**, *2*, 1165; b) J. Lin, B. T. Qiao, J. Y. Liu, Y. Q. Huang, A. Q. Wang, L. Li, W. S. Zhang, L. F. Allard, X. D. Wang, T. Zhang, *Angew. Chem.* **2012**, *124,* 2974–2978; *Angew. Chem. Int. Ed.* **2012**, *51*, 2920.

[31]   a) J. Bao, X. D. Zhang, B. Fan, J. J. Zhang, M. Zhou, W. L. Yang, X. Hu, H. Wang, B. C. Pan, Y. Xie, *Angew. Chem.* **2015**, *127*, 7507; *Angew. Chem. Int. Ed.* **2015**, *54*, 7399; b) X. D. Zhang, H. X. Li, X. T. Lv, J. C. Xu, Y. X. Wang, C. He, N. Liu, Y. Q. Yang, Y. Wang, *Chemistry-a European Journal* **2018**, *24*, 8822.

[32]   a) E. Tsuji, A. Imanishi, K. Fukui, Y. Nakato, *Electrochim. Acta* **2011**, *56*, 2009; b) D. Z. Wang, Z. P. Wang, C. L. Wang, P. Zhou, Z. Z. Wu, Z. H. Liu, *Electrochem. Commun.* **2013**, *34*, 219; c) D. W. Chen, C. L. Dong, Y. Q. Zou, D. Su, Y. C. Huang, L. Tao, S. Dou, S. H. Shen, S. Y. Wang, *Nanoscale* **2017**, *9*, 11969.

[33]   a) C. C. Chien, J. Z. Shi, T. J. Huang, *Ind. Eng. Chem. Res.* **1997**, *36*, 1544; b) W.-P. Dow, T.-J. Huang, *J. Catal.* **1996**, *160*, 171; c) D. Widmann, R. Leppelt, R. J. Behm, *J. Catal.* **2007**, *251*, 437; d) Z. Y. Pu, X. S. Liu, A. P. Jia, Y. L. Xie, J. Q. Lu, M. F. Luo, *J. Phys. Chem. C* **2008**, *112*, 15045; e) B. Yoon, H. Hakkinen, U. Landman, A. S. Worz, J. M. Antonietti, S. Abbet, K. Judai, U. Heiz, *Science* **2005**, *307*, 403.

[34]   G. Kresse, J. Furthmüller, *Phys Rev B Condens Matter* **1996**, *54*, 11169.

[35]   J. P. Perdew, J. A. Chevary, S. H. Vosko, K. A. Jackson, M. R. Pederson, D. J. Singh, C. Fiolhais,

1992, *46*, 6671.

[36]   G. Kresse, D. Joubert, *Phys. Rev. B* **1999**, *59*, 1758.

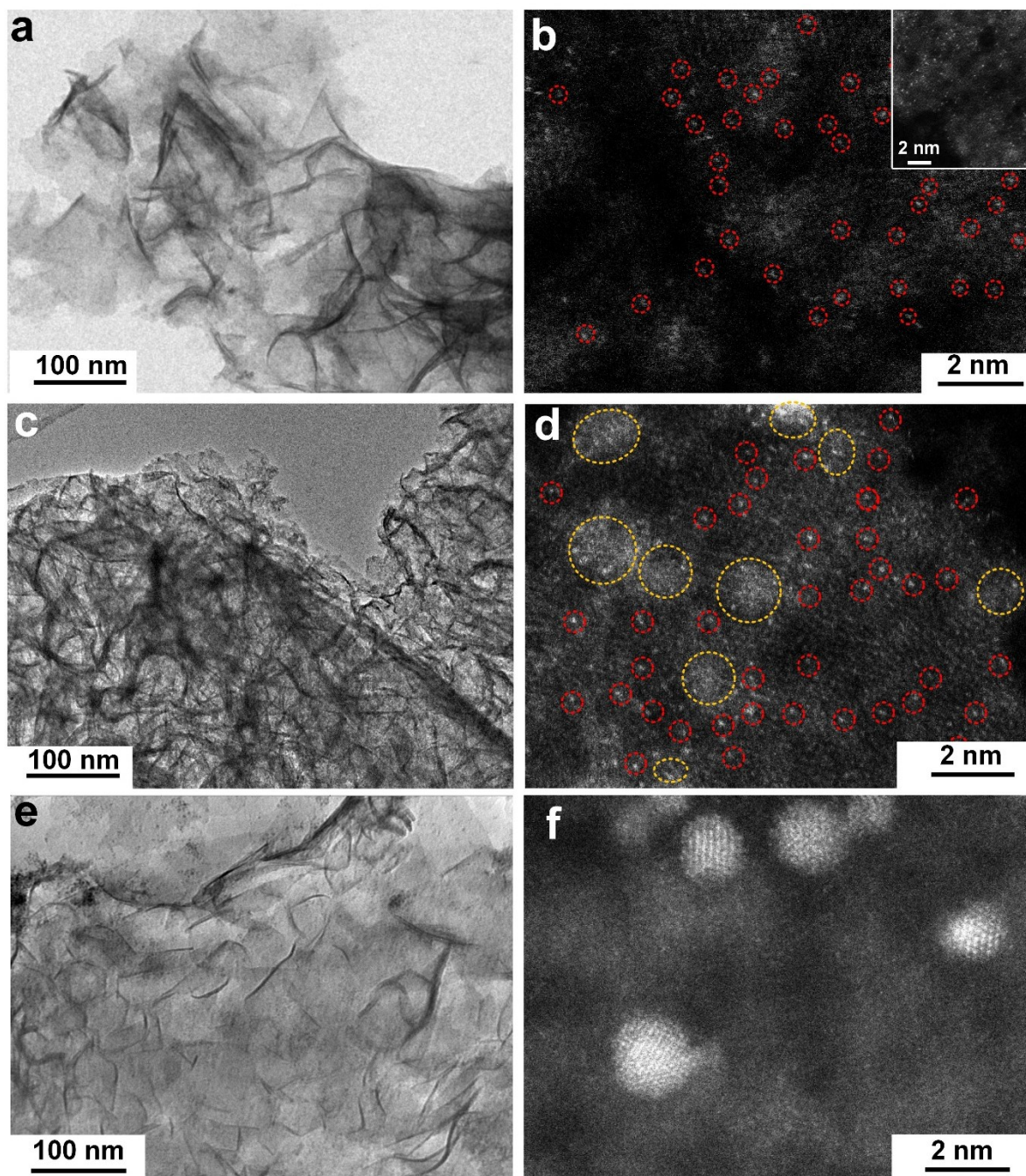[37]   H. J. Monkhorst, J. D. Pack, *Phys. Rev. B* **1976**, *13*, 5188.

Figure 1. Structural characterizations of amorphous Fe₂O₃ sheets with different Pt contents. (a) TEM image and (b) HAADF-STEM image of Pt-SA/A-Fe$_2$O$_3$. (c) TEM image and (d) HAADF-STEM image of Pt-SC/A-Fe$_2$O$_3$. The red circles represent the atomically dispersed single atom catalysts and the green circle is subnano atom clusters. (e) TEM image and (f)HAADF-STEM image of Pt-SN/A-Fe$_2$O$_3$.
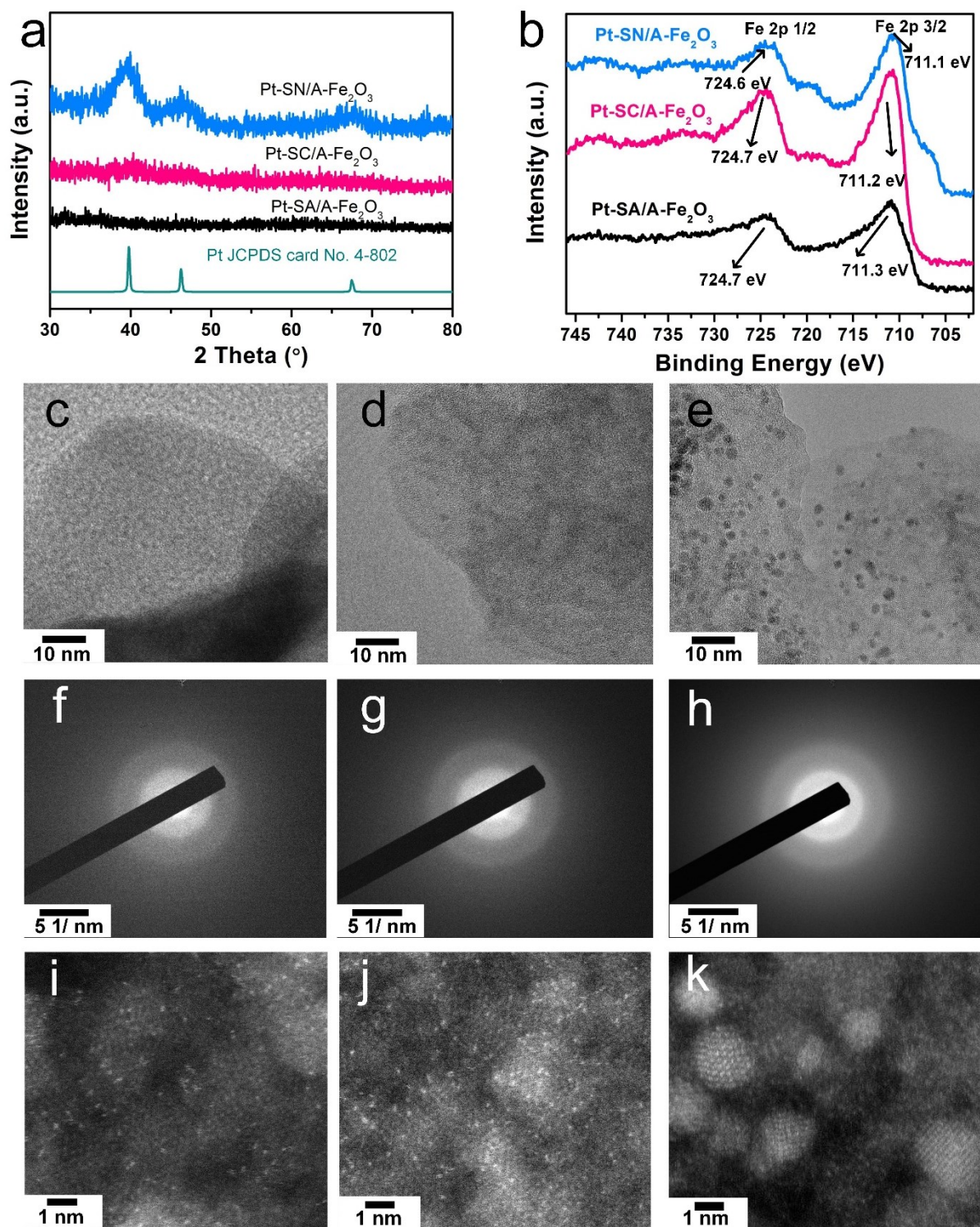
Figure 2. Nanoscale Structural characterizations of the three different Pt catalysts on the amorphous Fe₂O₃ support. (a) XRD and (b) XPS of as-prepared Pt-SA/A-Fe₂O₃, Pt-SC/A-Fe₂O₃, and Pt-

SN/A-Fe$_2$O$_3$. (c-e) HRTEM images, (f-h) the SAED pattern, and (i-k) the magnified HAADF-STEM image of Pt-SA/A-Fe$_2$O$_3$ (c,f,i), Pt-SC/A-Fe$_2$O$_3$ (d,g,j), and Pt-SN/A-Fe$_2$O$_3$ catalysts (e,h,k), respectively.
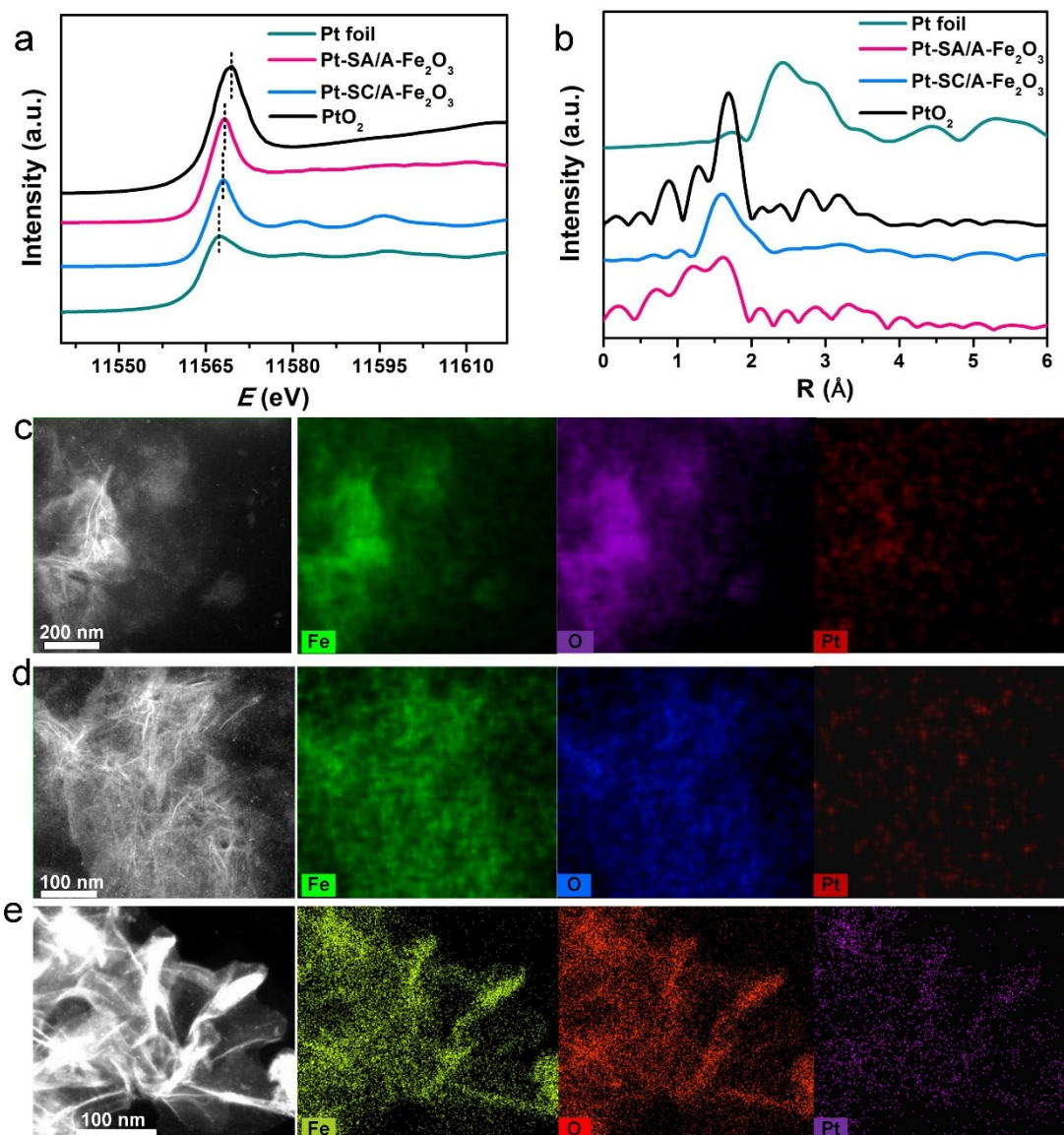
Figure 3. XAFS and EDX mapping study. Normalized (a) XANES and (b) EXAFS spectra of the Pt-SA/A-Fe$_2$O$_3$ and Pt-SC/A-Fe$_2$O$_3$, and the HAADF and corresponding STEM-EDS elemental mapping, of (c) Pt-SA/A-Fe$_2$O$_3$, (d) Pt-SC/A-Fe$_2$O$_3$, (e) Pt-SN/A-Fe$_2$O$_3$, respectively.
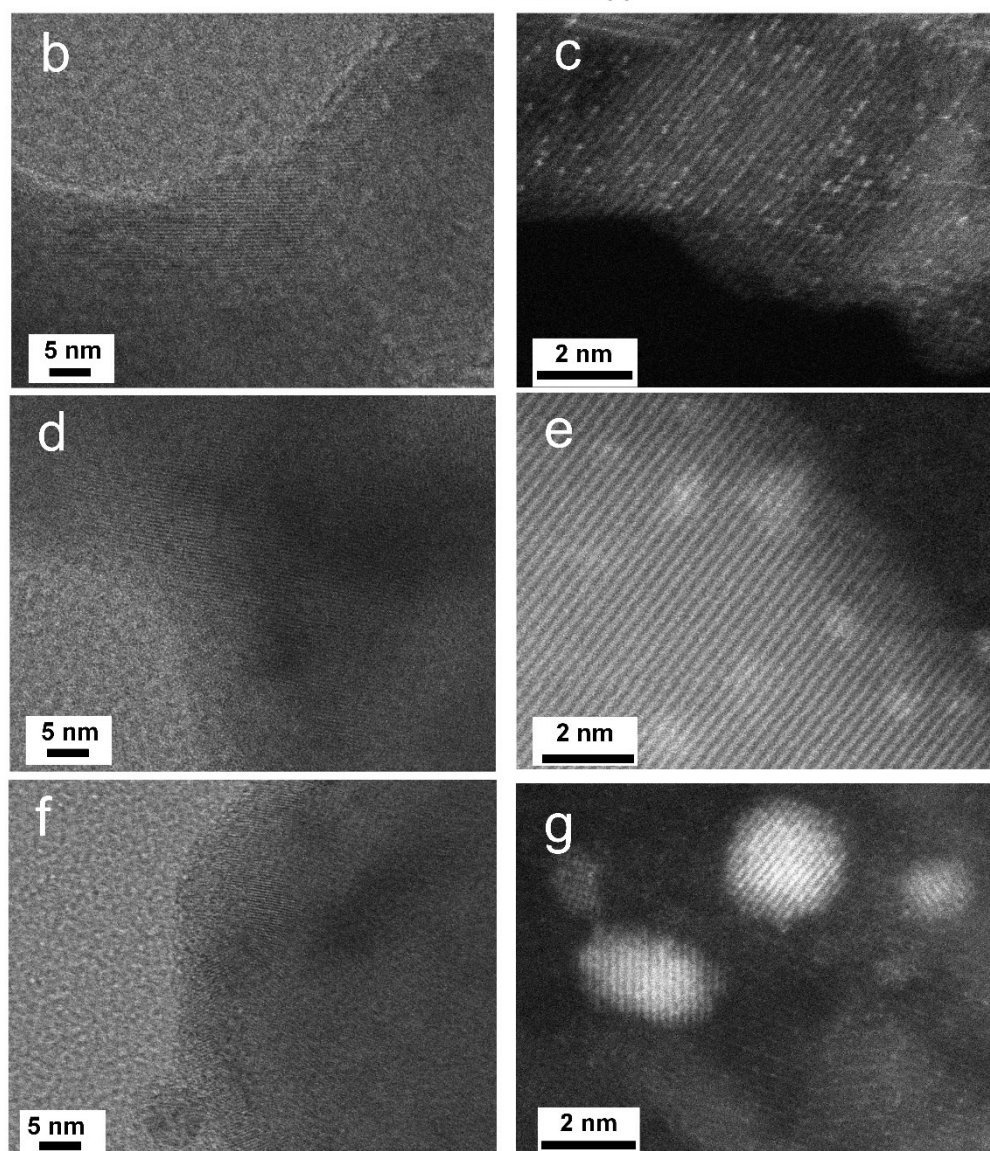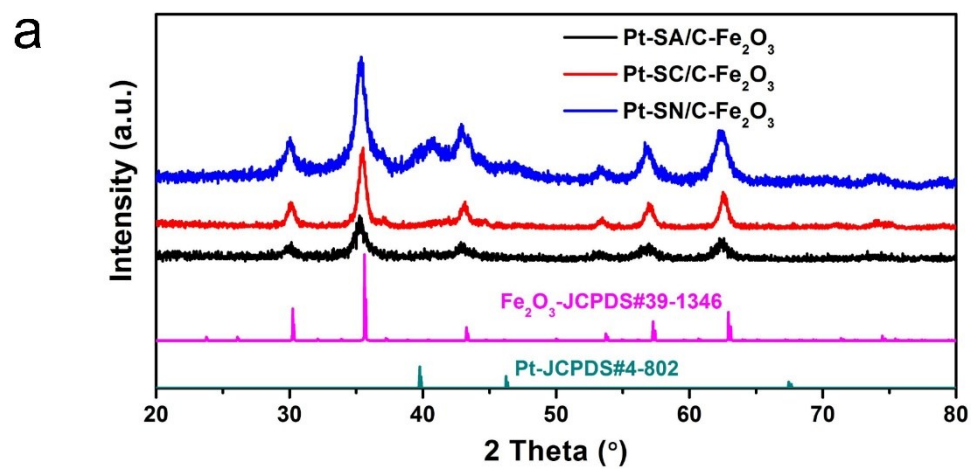
Figure 4. Structural characterizations of the three different Pt catalysts on the crystallized Fe₂O₃ support. (a) XRD pattern, (b, d, f) the HRTEM and (c, e, g) the corresponding HAADF-STEM images of the Pt-SA/C-Fe₂O₃ (b,c), Pt-SC/C-Fe₂O₃ (d,e), and Pt-SN/C-Fe₂O₃ (f,g), respectively.
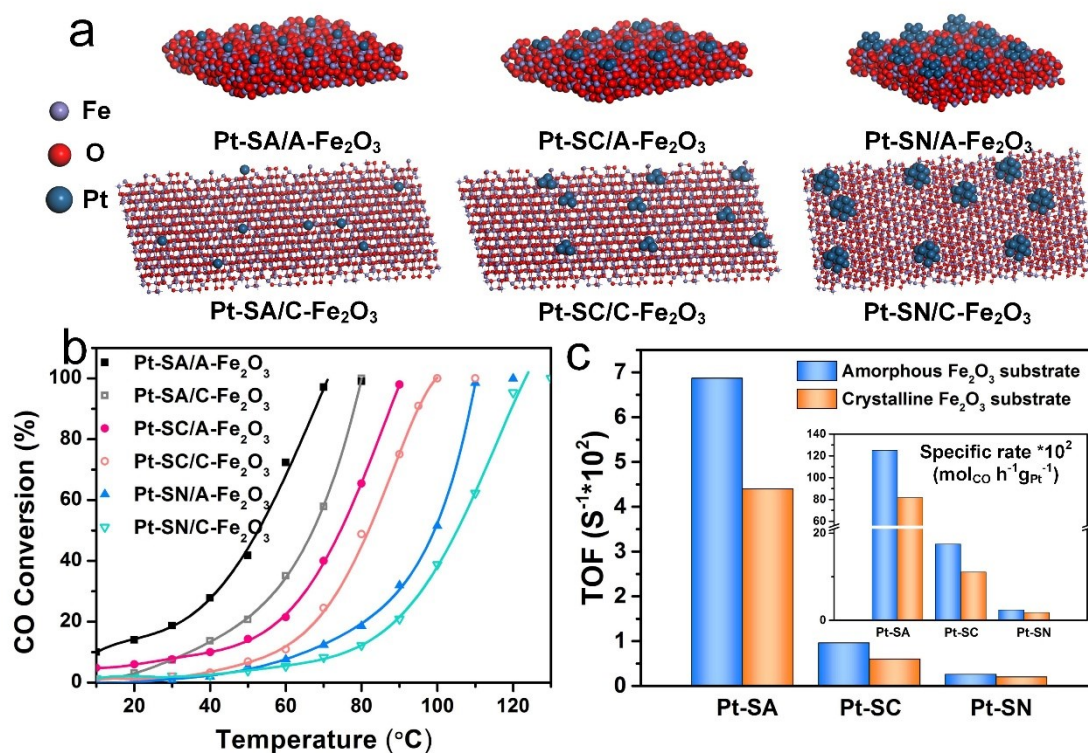

Figure 5. CO oxidation performance of the three different Pt catalysts on the two Fe₂O₃ supports. (a) Schematic of the different Pt/Fe₂O₃ structures, different sizes were used to distinguish the elements, (b) CO conversion, the different color curves represent the fitting curves for the CO performances based on the temperatures of different catalysts, respectively, (c) TOFs and specific rates (inset).

a △q: 0.746 e^-

b △q: 0.221 e^-

c △q: 0.114 e^-

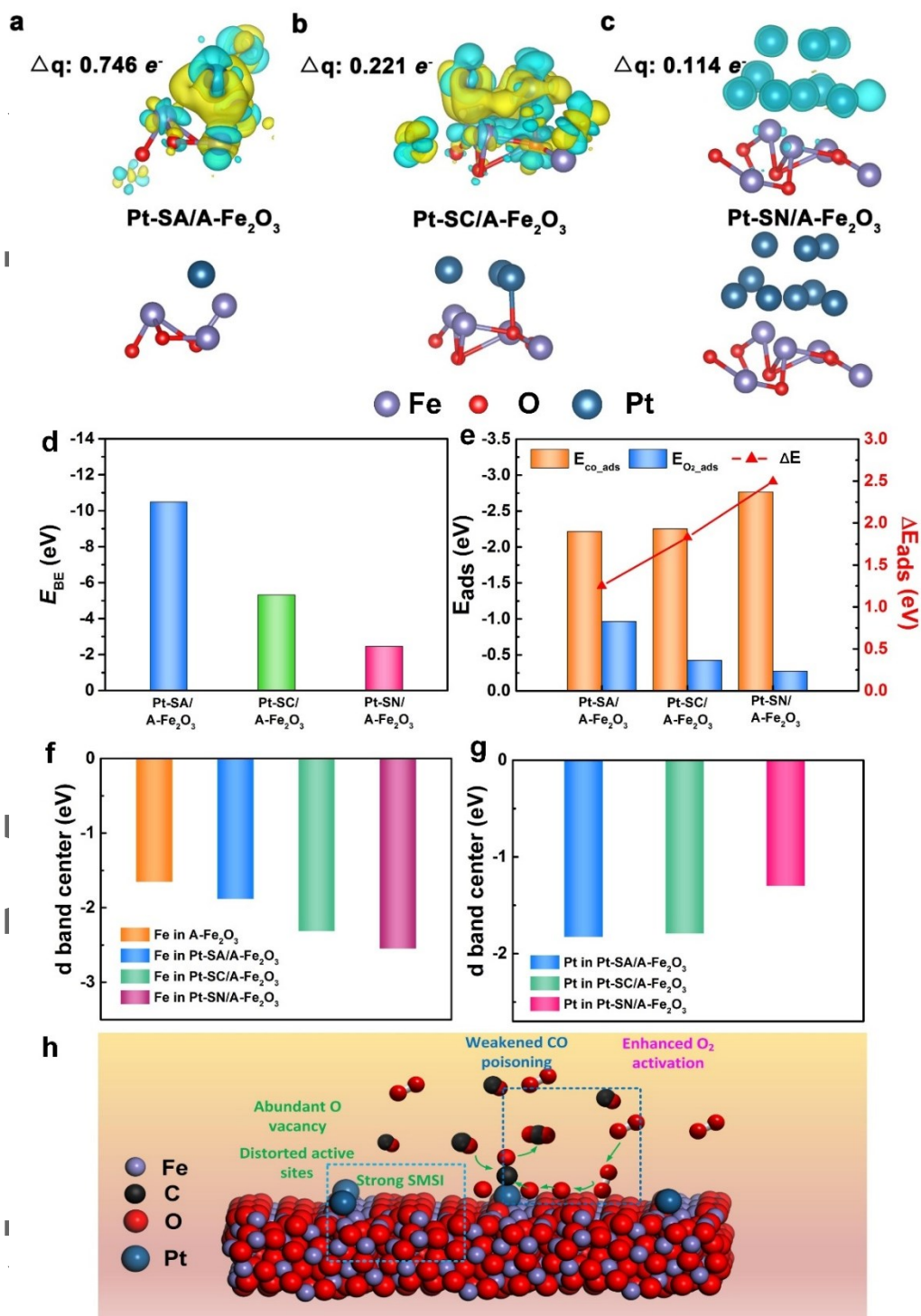Pt-SA/A-Fe$_2$O$_3$ Pt-SC/A-Fe$_2$O$_3$ Pt-SN/A-Fe$_2$O$_3$

Fe   O   Pt

Figure 6. DFT calculation of the electrons transfer and adsorption energy. Charge density difference and the separate atomic model of (a) Pt-SA/A-Fe$_2$O$_3$, (b) Pt-SC/A-Fe$_2$O$_3$ and (c) Pt-SN/A-Fe$_2$O$_3$,

respectively. Yellow regions represent electron depletion and blue ones denote electron accumulation with an isosurface value of 0.1 electrons/$Å^3$. Numerical values are given in units of e based on Bader charge analysis. (d) The binding energy between Pt-SA/A-Fe_2O_3, Pt-SC/A-Fe_2O_3 and Pt-SN/A-Fe_2O_3. (e) The stable adsorption energy of CO and O_2 for Pt-SA/A-Fe_2O_3, Pt-SC/A-Fe_2O_3, Pt-SN/A-Fe_2O_3, and the energy difference ΔE between E_{ads-CO} and E_{O2-ads}, (f) the comparison among of d-band center of Fe in A-Fe_2O_3 and the three different catalysts, (g) the comparison of d-band center of Pt in the three different catalysts, and (h) mechanism and process CO oxidation on Pt-SA/A-Fe_2O_3.

Table 1. Comparison of specific rates and TOFs of different Pt/Fe_2O_3 catalysts at 70 ºC

Samples	Pt loading wt%	d_{Pt}(nm)	specific rate × 10^2, mol_{CO} h^{-1} g_{Pt}^{-1}	TOF × 10^2, s^{-1}
Pt-SA/A-Fe_2O_3	1.2	-	125.0	6.87
Pt-SC/A-Fe_2O_3	4.6	~1.2	17.5	0.96
Pt-SN/A-Fe_2O_3	8.62	~2	2.37	0.26
Pt-SA/C-Fe_2O_3	1.2	-	81.6	4.4
Pt-SA/C-Fe_2O_3	4.6	~1.2	11.07	0.60
Pt-SA/C-Fe_2O_3	1.2	~2	1.78	0.20

Note: TOF was calculated based on Pt dispersion (mol CO_{ox}/mol surface Pt). All the single atom Pt atoms were used for calculation for Pt-SA/A-Fe_2O_3 and Pt-SA/C-Fe_2O_3. Pt dispersion of Pt-SC/A-Fe_2O_3, Pt-SN/A-Fe_2O_3, Pt-SC/C-Fe_2O_3 and Pt-SN/C-Fe_2O_3 were estimated by the Pt size according to D = $1/d_{Pt}$.

An atomically dispersed catalyst that consists of single Pt atoms anchored to the surfaces of amorphous Fe_2O_3 nanosheets. The size effect of Pt and phase effect of support are explored. The synergistic effect resulted from the strong binding and stabilization of single Pt atoms with the SMSI between the single Pt atoms and amorphous Fe_2O_3 supports lead to an enhanced CO oxidation performance.

single atom, amorphous, CO oxidation, Fe_2O_3, Pt

Wenlong Chen, Yanling Ma, Fan Li, Lei Pan, Wenpei Gao, Qian Xiang, Shang Wen, Chengyi Song, Peng Tao, Hong Zhu, Xiaoqing Pan, Tao Deng, Jianbo Wu*

Strong Electronic Interaction of Amorphous Fe_2O_3 Nanosheets with Single Atom Pt towards Enhanced Carbon Monoxide Oxidation